

Three-dimensional optical tomographic imaging of vascular reactivity in the brain

Andreas H. Hielscher^{*a,b}, Avraham Y. Bluestone^a, Gassan S. Abdoulaev^a,
Joseph Lasker^{a,b}, Randall L. Barbour^{a,b}, Christoph H. Schmitz^a

^aDept. of Pathology, State Univ. of New York - Downstate Medical Center, Brooklyn NY 11203

^bDept. of Electrical and Computer Engineering, Polytechnic University, Brooklyn NY 11201

ABSTRACT

We report on the first three-dimensional, volumetric, tomographic localization of changes in the concentration of oxyhemoglobin and deoxyhemoglobin in the brain. To this end we have developed a model-based iterative image reconstruction scheme that employs adjoint differentiation methods to minimize the difference between measured and predicted data. To illustrate the performance of the technique, the three-dimensional distribution of changes in the concentration of oxyhemoglobin and deoxyhemoglobin during a Valsalva maneuver are visualized. The observed results are consistent with previously reported effects concerning optical responses to hemodynamic perturbations.

Keywords: Optical tomography, brain imaging, volumetric imaging, blood/tissue constituent monitoring

1. INTRODUCTION

Several groups are currently pursuing the possibility of imaging the brain with diffuse optical tomography (DOT) [1-15]. Applications range from functional imaging [2-4,7,14] to the detection of hematomas [6,15]. For example, Benaron *et al.* studied physiological changes in brain oxygenation in male adults during mixed motor and sensory cortex activation [1]. Hoshi *et al.* [2] obtained quantitative images of hemoglobin concentration changes associated with neuronal activation in the human brain during a forward (DF) and backward (DB) digit span task, which assesses verbal working memory. Watanabe *et al.* have developed an optical system for obtaining 2-dimensional maps pinpointing the location of epileptic foci [3], and Franceschini *et al.* have reported on imaging arterial pulsation and motor activation in healthy human subjects [4]. These and other works clearly have established that near-infrared light can be used to probe the brain for changes in blood oxygenation and blood volume.

In most of the currently established protocols, either a single source and a single detector is used to perform point measurements, or an array of sources and detectors with a fixed geometry is employed to obtain topographic maps. These maps project the cortical response during various protocols together with the superficial vascular changes onto a two-dimensional surface map. Results are usually obtained by back-projecting measured light intensities between corresponding source-detector pairs multiplied by the appropriate pathlength factor to obtain the change in the absorption coefficients along the path [2,4].

The goal of this work is to go beyond topographic maps and obtain three-dimensional, volumetric reconstructions of the changes in optical properties inside a human head. To this end we have developed a model-based iterative image reconstruction (MOBIIR) scheme that uses a finite-element formulation of the three-dimensional, time-independent diffusion equation as a forward model. To illustrate the performance of this approach we demonstrate a volumetric reconstruction of the vascular reactivity in the brain during a Valsalva maneuver.

* As of September 1, 2001, the author is with Columbia University, Departments of Biomedical Engineering and Radiology, 416 CEPSR-Schapiro Bldg., MC 8904, 530 West 120th Street, New York, NY 10027, email: ahielscher@downstate.edu.

2. METHODS

2.1 Image Reconstruction Algorithm

In this work the 3-dimensional reconstruction of the optical properties in the human head was achieved using a model-based iterative image reconstruction (MOBIIR) scheme [16-19]. Our MOBIIR scheme comprises three major parts: (1) a forward model that predicts the detector readings based on a given spatial distribution of optical properties, (2) an objective function Θ that compares predicted with measured signals, and (3) an updating scheme that uses the gradient of the objective function with respect to the optical properties to provide a means of updating the optical parameters for subsequent forward calculations.

The forward model that we employ is the time-independent diffusion equation with Robin boundary conditions along all exterior surfaces. The finite element forward model is similar to works that have already been described by other groups [20,21]. The domain Ω is divided into P elements, joined at N vertex nodes. The solution is approximated by a piecewise function spanned by a set of linear basis functions. The solution is obtained by sparse matrix inversion using the preconditioned conjugate gradient method [22]. Two added features allow for internal mesh refinement and multigrid capabilities [23].

The objective function that determines the goodness-of-fit between measured data, M , and predicted detector data, P , has consistently been defined by many groups as

$$\Theta = \sum_s \sum_d \frac{(M_{s,d} - P_{s,d})^2}{\sigma_{s,d}^2} \quad (1)$$

where s , d refer to sources and detectors, respectively and σ is the standard deviation [16-19]. However, in order to deal with data generated via a difference measurement approach, the objective function must be modified. In a difference measurement approach one is unable to determine the absolute detector readings for a single time point and hence must compare the change in detector readings between two states; a pre and post perturbation state. This method has two main advantages: first, it is less sensitive to boundary effects and second; it is less sensitive to the initial guess chosen for the background medium [24]. Its major disadvantage is that one cannot determine the true distribution of optical properties, only the change in the absorption coefficient, μ_a , the reduced scattering coefficient μ_s' , or the diffusion coefficient, $D = c/3(\mu_a + \mu_s')$ from baseline. However, many groups have used this approach for localizing brain activity and for determining general trends in the oxygenation state [1,8,25].

To deal with difference data, we have adapted an approach first proposed by Y. Pei et al. [24], and modified the objective function defined in Eq. (1) to yield

$$\Theta = \sum_s \sum_d \frac{\left[\left(\frac{M_{s,d}^{pert(t)}}{M_{s,d}^{ref}} P_{s,d}(\xi_0) \right) - P_{s,d}(\xi_n) \right]^2}{\left(\frac{M_{s,d}^{pert(t)}}{M_{s,d}^{ref}} P_{s,d}(\xi_0) \right)^2}. \quad (2)$$

Here the relative changes $(M_{s,d}^{pert} / M_{s,d}^{ref})$ are multiplied with the predicted detector readings $P_{s,d}$ obtained from an initial distribution $\xi_0 := (\mu_{a,0}, D_0)$ of the optical properties (typically assumed to be homogeneous). In subsequent iterations a distribution $\xi := (\mu_a, D)$ is sought that produces the prediction $P_{s,d}(\xi)$ that most closely matches $(M_{s,d}^{pert} / M_{s,d}^{ref}) P_{s,d}(\xi_0)$. The resulting distribution ξ is then a spatial representation of the differences in optical properties that led to the differences measured between $M_{s,d}^{pert}$ and $M_{s,d}^{ref}$. Generally, one can look at the difference between rest $M_{s,d}^{ref}$ and

corresponding time points $M_{s,d}^{pert(t)}$ during a perturbation, where s and d refer to sums over all sources and detectors, respectively.

The image reconstruction process is started with an initial guess of optical properties, in our case $\xi_0 = (\mu_a = 0.1 \text{ cm}^{-1}, D = 1.0 \text{ cm}^2\text{ns}^{-1})$. Using this initial guess the detector readings $P_{s,d}(\xi_0)$ are calculated with the finite element forward solver over the domain of interest, and the value of the objective function is determined. To update the initial distribution of optical properties, one must calculate the gradient of the objective function with respect to all optical properties $(\partial\Theta/\partial\mu_a, \partial\Theta/\partial D)$. This gradient defines a direction of minimum descent, which is then used in a multidimensional conjugate gradient descent algorithm that minimizes the objective function [16, 17].

The calculation of the gradient was performed using the technique of adjoint differentiation [16, 17, 18, 26, and 27]. In particular we adapted an approach by Roy et al [18]. In this case, the computational burden for the gradient calculation is on the order of one forward calculation. The objective function and gradient algorithm is incorporated in a multidimensional conjugate gradient descent algorithm where typically 15-30 iterations with different gradients are necessary before convergence is achieved.

2.2 Determination of surface coordinates and mesh generation

For model-based optical tomographic imaging reconstructions one has to determine the surface geometry and source-detector locations. To achieve this we employed the techniques of photogrammetry [28, 29, 30]. To determine the 3-D coordinates of the surface of the forehead as well as all source-detector locations we placed circular reflective markers on the head. These markers, because of their circular shape, have the advantage of allowing sub-pixel precision when used in combination with the centroid-locating algorithm. Because the surface of the forehead can be approximated as a smooth surfaced contour, it is acceptable to place a sparse distribution of points over the surface of the head and use non-uniform B-splines (Nurbs) [31] to connect them. Other approaches, such as the use of holographic imaging or laser surface scanning devices are also feasible. However, the technical complexity paired with their high costs make them less practical and appealing in a day-to-day clinical setting.

Once all markers were placed on the surface of the head, the area of interest was photographed from different angles with a digital camera (SONY Mavika FD-90). These images of the head were then transferred to a desktop computer for analysis with the commercially available Photogrammetry software package (Photomodeler, Eos Systems Inc., Vancouver, Canada). After the targets in the photographs were marked and referenced we processed the images using the bundle adjustment algorithm, which computed all 3D coordinates of all referenced points. The resulting coordinates on average have an accuracy of 0.023 cm with a standard deviation of 0.004; however, this is dependent on the number of points referenced and on the maximum angle between the multiple camera positions [30].

Having generated the surface coordinates of the human head, the boundary of our domain, it was necessary to build the corresponding volume. To this end, the coordinates of the surface points obtained using the photogrammetric approach were exported to a volumetric mesh generator. For this procedure, we used the CAD style volume generator GID software package (GID, CIMNE Inter. Center for Num. Methods, Barcelona, Spain). This package allowed us to manually extend the surface in the z direction by 4.0 cm and build the corresponding volume mesh, which are required for the reconstruction. Since computational time depends on the number of mesh nodes, we limited the volume to a 4.0 cm zone beneath the surface of interest, and not to the entire head. We found that larger volumes are not necessary to consider, since their influence on the reconstruction results is negligible. More details on the photogrammetry approach and the mesh generation can be found in reference [32].

2.4 Instrumentation and data acquisition

Measurements on the human forehead are performed with the dynamic near-infrared optical tomography instrument, recently developed by Schmitz *et al.* [33,34]. This instrument operates in continuous-wave mode. A beam from each laser diode is coupled into a set of source fiber bundles. Two laser diodes one of 760nm and the other of 830nm are

modulated at 5KHz and 7KHz, respectively. The demodulated signal allows for the simultaneous measurement of the intensity at all detectors for a given source position at both wavelengths. Having this dual-wavelength capability allows for the elucidation of both oxyhemoglobin and deoxyhemoglobin, as will be described further in section 2.5. For the measurements presented in this work we used 4 sources and 15 detectors, resulting in 60 source-detector combinations. Three tomographic data sets, involving all 60 source-detector pairs, were acquired per second.

2.5 Experimental Protocol

The experiment was designed to look at functional hemodynamic changes in the forehead of a single patient induced by a Valsalva maneuver. For the measurement the patient was placed in the supine position. Three epochs consisting of Valsalva maneuvers with one-minute rest periods interspersed were performed. During the Valsalva maneuver a forced expiration against a closed glottis demonstrates the effects of changes in intrathoracic pressure on blood pressure, and the brain's autoregulatory response to decreased vascular perfusion pressure in cerebral vessels [35].

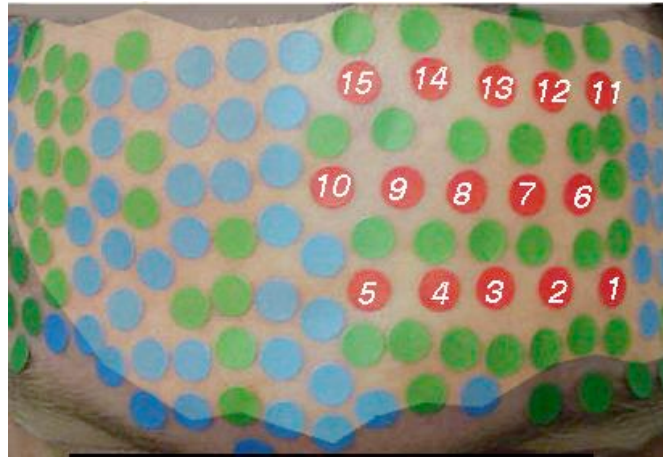


Fig. 1: Placement of sources and detectors on forehead. The 15 source/detector positions are indicated by the encircled numbers. Other round dots indicate reference points used for the photogrammetric surface determination. The lighter shaded area depicts the outer surface of the finite-element mesh, which was used for the volumetric image reconstruction.

Figure 1 shows the locations of the sources and detectors on the forehead. A three-tiered band was used to secure 3 sets of 5 optodes per tier to the left forehead. Each optode consisted of a co-located source and detector, and all measurements were performed simultaneously at 760nm and 830 nm. Assuming that the primary influences on the changes in the absorption coefficients at each wavelength are a linear combination of oxyhemoglobin and deoxyhemoglobin, one arrives at [36,37]

$$\Delta\mu_a^\lambda = \epsilon_{HbO}^\lambda \Delta[HbO] + \epsilon_{Hb}^\lambda \Delta[HbO]. \quad (3)$$

By simultaneously solving a set of algebraic equations at the disparate wavelengths ($\lambda_1, \lambda_2, \dots, \lambda_n$), it is possible to calculate the true concentrations of the, n , chromophores of interest. For the case of two chromophores consisting of oxyhemoglobin and deoxyhemoglobin the set of equations are:

$$\Delta[Hb]_{meas} = \frac{\epsilon_{HbO}^{\lambda_2} \Delta\mu_a^{\lambda_1} - \epsilon_{HbO}^{\lambda_1} \Delta\mu_a^{\lambda_2}}{\epsilon_{Hb}^{\lambda_1} \epsilon_{HbO}^{\lambda_2} - \epsilon_{Hb}^{\lambda_2} \epsilon_{HbO}^{\lambda_1}}, \quad (4)$$

$$\Delta[HbO]_{meas} = \frac{\epsilon_{Hb}^{\lambda_2} \Delta\mu_a^{\lambda_1} - \epsilon_{Hb}^{\lambda_1} \Delta\mu_a^{\lambda_2}}{\epsilon_{Hb}^{\lambda_1} \epsilon_{HbO}^{\lambda_2} - \epsilon_{Hb}^{\lambda_2} \epsilon_{HbO}^{\lambda_1}}. \quad (5)$$

where λ indicates the wavelength, \mathcal{E}_{Hb} and \mathcal{E}_{HbO} are the known extinction coefficients for deoxyhemoglobin and oxyhemoglobin at the given wavelengths [37], respectively. The $\Delta\mu_a$'s in Eqs 4 and 5, at each of the two wavelengths, are the calculated changes in the absorption coefficients at each node of the mesh determined using the reconstruction algorithm. The reconstruction algorithm accounts for the path length between given source detector positions and reconstructs the predicted $\Delta\mu_a$'s at each node. By solving Eqs. (4) and. (5) the changes in oxyhemoglobin, $\Delta[HbO]_{\text{meas}}$, and deoxyhemoglobin, $\Delta[Hb]_{\text{meas}}$, can be determined.

3. RESULTS

A trace of the measured output produced by the optical image system for the three Valsalva epochs is shown in Fig. 2. Displayed are fifteen traces of the normalized (to the rest period) and smoothed measured intensity profile during the three consecutive Valsalva maneuvers for source position three at a wavelength of 760nm.

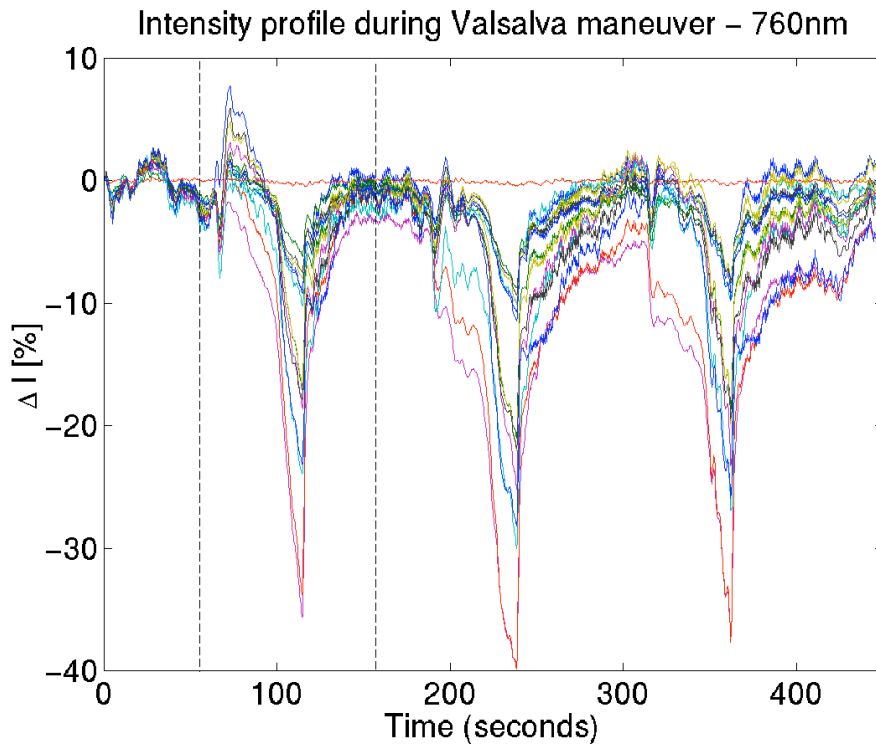


Fig. 2: Time series of 15 detector readings during three successive Valsalva maneuvers. The source was located at position three (see Fig. 1). Each Valsalva maneuver was followed by a rest period. The measurements displayed were performed with near-infrared light at $\lambda = 760\text{nm}$.

It can be seen that the Valsalva maneuver protocol is very reproducible from epoch to epoch, and a strong signal drop in all detectors can be observed. At the peak of the Valsalva maneuver the measurement intensities changed with respect to the rest period by up to 40%.

To enhance the signal to noise ratio a median filter given by

$$x_i = \frac{1}{2\delta} \sum_{k=i-\delta}^{k=i+\delta} x_k \quad (6)$$

was used to smooth the intensity profile. This median filter sets the value at a given point to the average value of its δ neighbors. In this work we chose $\delta = 2$, which produced a smooth function without much distortion in the overall intensity profile (Fig. 3). For our three-dimensional reconstructions we focused on the data during the first of the three epochs, which are displayed in Fig. 3. At $t = 10$ seconds the Valsalva maneuver began. Initially an increase in signal was observed, which returned to baseline within 10-15 seconds. Then the signal decreased steadily and approached a minimum at $t = 65$ seconds at which point the Valsalva maneuver was stopped. The signal rapidly recovers and eventually returns to base line.

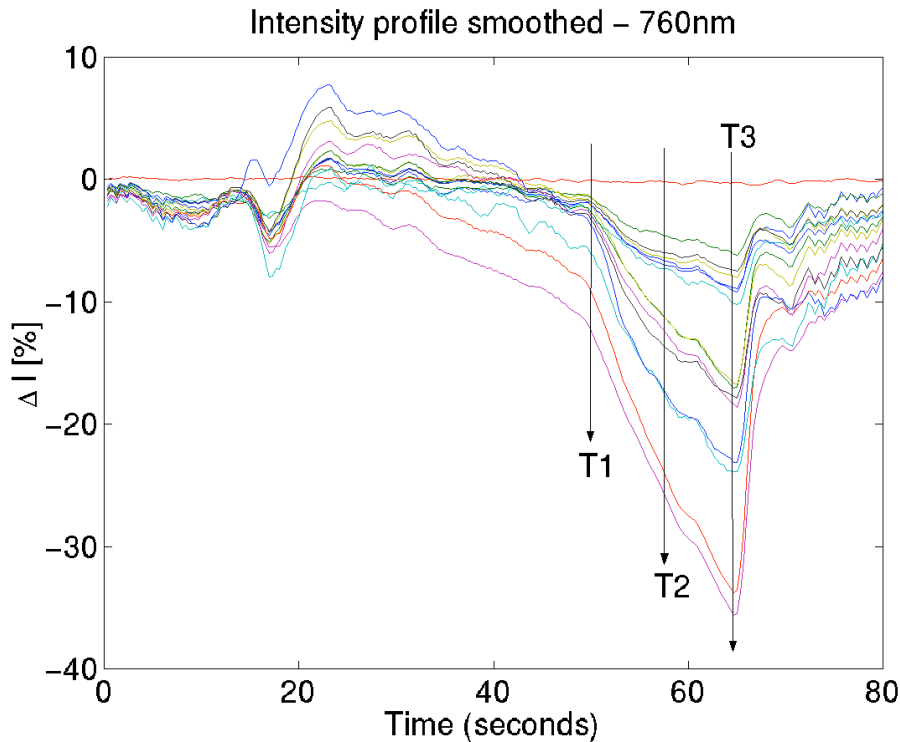


Figure 3: Median-filtered time series for first Valsalva maneuver epoch seen in Fig. 2.

For the difference reconstruction we used the ratio of the data at the time points T1, T2, and T3, with respect to data at time point $t = 0$ (Fig. 3). We chose these points because during this period the signal undergoes strong changes and strong effects in the expected hemodynamics. Figures 4-6 show the three-dimensional distribution of the reconstructed values for changes in deoxyhemoglobin (Hb) and oxyhemoglobin (HbO_2) at all three time points. All reconstructions were stopped after 25 iterations. At this point no further changes in the reconstructed distributions were observed. The 25 iterations for each image took approximately 4 hours on a Pentium III 550Mhz processor. Displayed are volumetric reconstructions for three different views: frontal (standing in front of body and looking towards the face), side (standing next to body and looking towards the right ear), and aerial (looking from top of the head down towards the body). The different colors (shadings) represent isosurfaces of constant oxyhemoglobin and deoxyhemoglobin concentration changes relative to the reference point at $t = 0$.

In Fig. 4 (corresponding to time point T1) small increases in both Hb and HbO_2 at two discrete locations can be observed. The increase in HbO_2 is about 3 times larger than the increase in Hb ($\sim 0.01\text{mM}$ versus 0.003mM). In Fig. 5 (time T2) the two separate regions in the Hb image have merged to become a larger connected region, in which $\Delta Hb > 0.003\text{mM}$ throughout. In one area, close to the center of the forehead, changes in deoxyhemoglobin reach values of $\Delta Hb > 0.019\text{mM}$. The change in oxyhemoglobin reaches values of $\Delta HbO_2 > 0.06\text{mM}$. In the cluster of areas in-between the originally appearing two regions (Fig. 4) the oxyhemoglobin concentration slightly drops by more than 0.01mM . In Fig. 6 (time T3) the deoxy- and oxy-hemoglobin changes just before the end of the Valsalva maneuver are shown. Two major regions of deoxygenation have evolved in which ΔHb -values of up to $+0.047\text{mM}$ can be found. Oxyhemoglobin values have changed by as much as 0.12mM in the center and the upper right corner of the forehead.

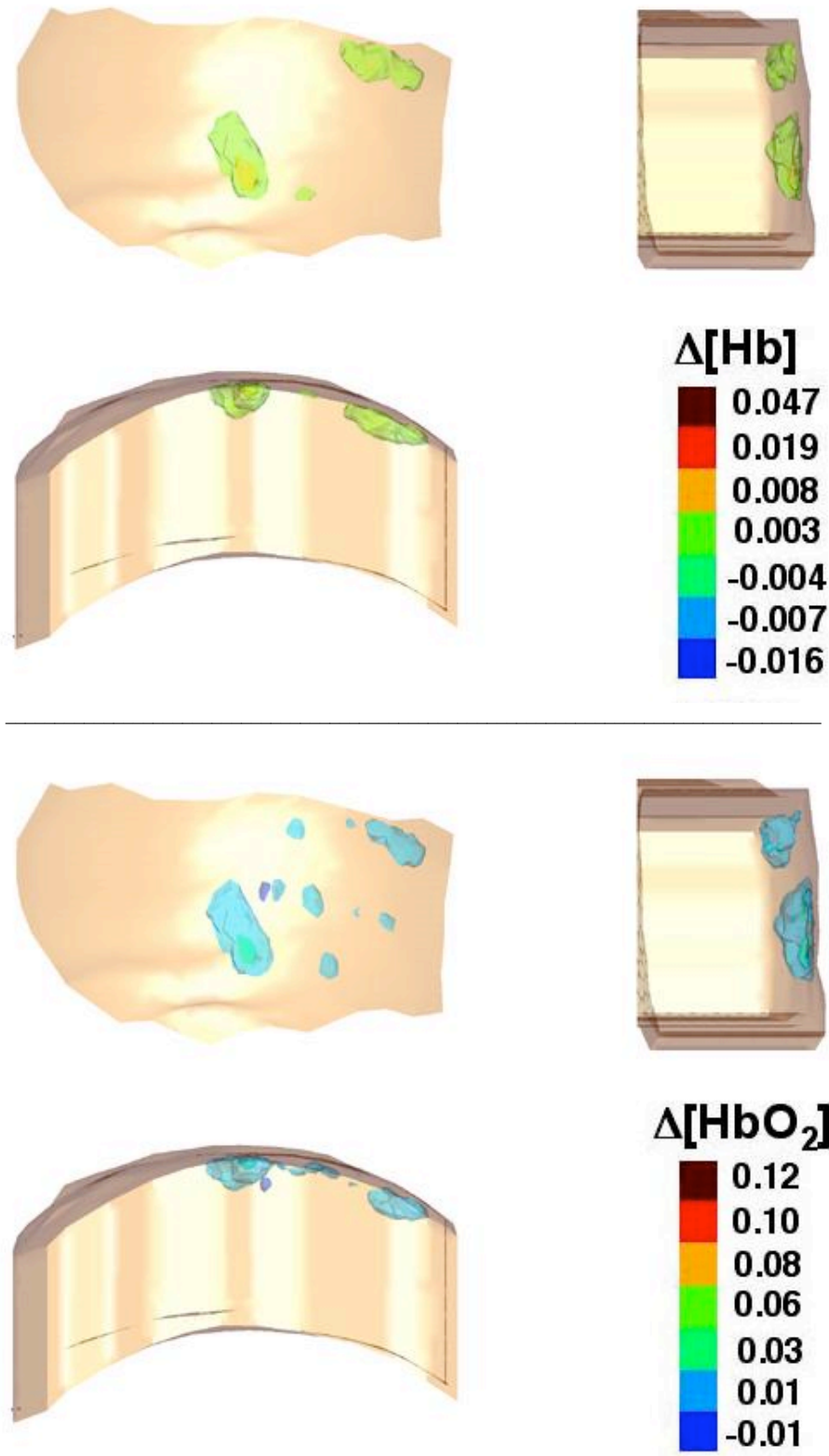


Fig. 4: Reconstructed changes in deoxyhemoglobin (top) and oxyhemoglobin (bottom) at time T1 (see Fig.3) during a Valsalva maneuver. The changes are given in units of [mM]. Shown are a frontal view (upper left), a side view (upper right), and an aerial or birds-eye view (lower left) of the forehead.

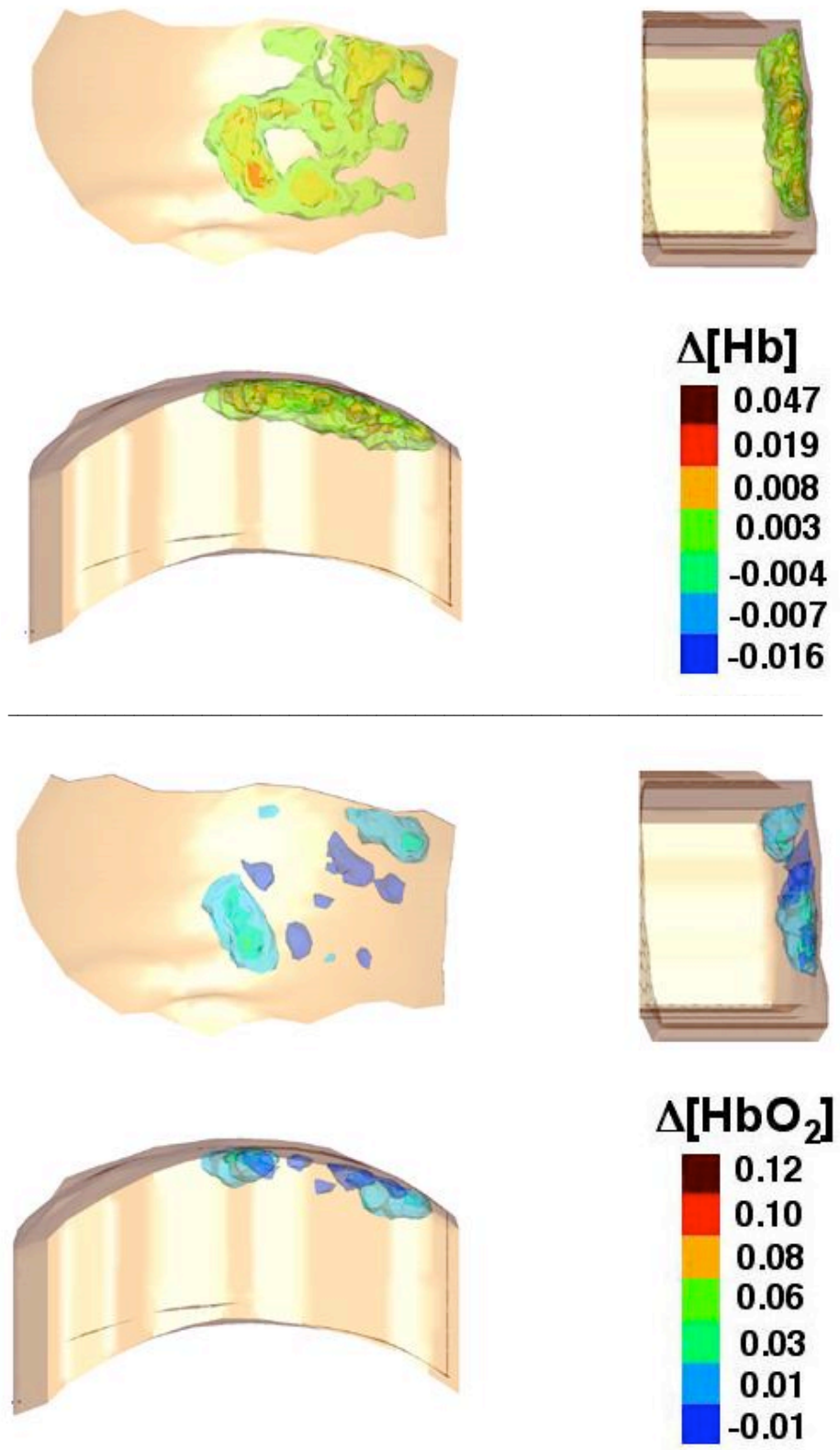


Fig. 5: Reconstructed changes in deoxyhemoglobin (top) and oxyhemoglobin (bottom) at time T2 (see Fig.3) during a Valsalva maneuver. The changes are given in units of [mM]. Shown are a frontal view (upper left), a side view (upper right), and an aerial view (lower left) of the forehead.

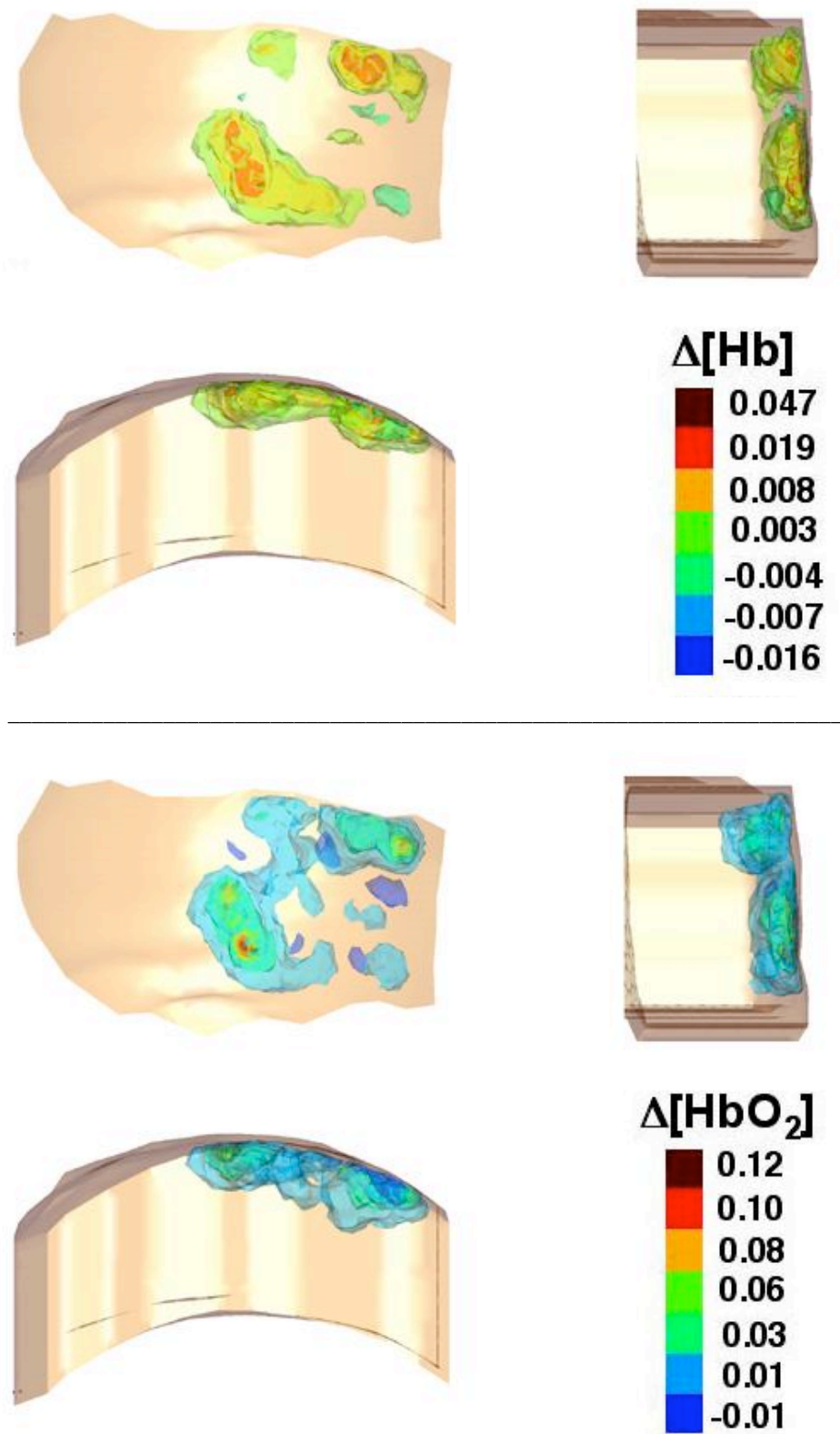


Fig. 6: Reconstructed changes in deoxyhemoglobin (top) and oxyhemoglobin (bottom) at time T3 (see Fig.3) during a Valsalva maneuver. The changes are given in units of [mM]. Shown are a frontal view (upper left), a side view (upper right), and an aerial view (lower left) of the forehead.

These findings are consistent with previously reported effects concerning optical responses to hemodynamic perturbations. Specifically, those groups measuring functional tasks record optical signal changes of approximately 0.2% to a maximal of 5%. These signal changes were related to concentration changes of oxyhemoglobin, as shown in the topographic maps, from $\Delta HbO_2 = -0.002$ to $\Delta HbQ = 0.003$ mM [4]. In this study we show that the Valsalva maneuver leads to changes in the measured optical signal from 1 to 50%, which is about 25 times stronger than during functional activation. These optical signals are related to an approximately 5-40 times as large concentration change of oxyhemoglobin, which lies between $\Delta HbO_2 = -0.01$ and $\Delta HbO_2 = 0.12$ mM. Furthermore, we observe that the ratio of the concentration change of oxyhemoglobin to deoxyhemoglobin is in the range of 3 to 6. This finding is also consistent with the observation made by Franceschini [4] and others. Hoshi et al. [2] notes that the oxyhemoglobin signal is the more sensitive parameter of activity-dependent changes in regional cerebral blood flow.

4. SUMMARY

In this paper we have reported on the first volumetric reconstructions of changes in oxyhemoglobin and deoxyhemoglobin in the human forehead using a 3-dimensional model-based iterative image reconstruction (MOBIIR) scheme. To achieve this goal we placed a three-tiered band over a patient's left forehead and performed measurement during a Valsalva maneuver. A photogrammetric method was used to determine the surface geometry over the external contour of the forehead and the exact location of our optodes. Having accurately defined the surface geometry, we exported this data to a finite element mesh generator where we constructed a subsurface volume of the head region based on the aforementioned surface coordinates. This information together with the measurement data performed on the forehead became input to the diffusion-based finite-element inverse solver. Finally, we presented 3-dimensional tomographic reconstructions of the changes in oxyhemoglobin, deoxyhemoglobin, and volume in the human forehead. This protocol allowed us to determine the plausibility of using DOT to determine the global changes in oxyhemoglobin and deoxyhemoglobin in the human head. Ultimately, we would hope to dynamically assess the cerebral autoregulatory mechanism that maintains constant cerebral blood flow within a wide range of cerebral perfusion pressures. As is well known, the clinical importance of assessing the cerebral autoregulatory mechanism lies in the protection of the brain from the sequelae of arterial hypotension and hypertension and ultimately in the diagnosis of cerebrovascular disease [35,38].

ACKNOWLEDGMENTS

This work was supported in part by the New York City Council Speaker's Fund for Biomedical Research: Toward the Science of Patient Care, an SBIR grant from the National Heart, Lung, and Blood Institute (NHLBI) (grant # 2R44-HL-61057-02), and funds from the National Cancer Institute (grant # R01-CA 66184), which are both part of the National Institutes of Health.

REFERENCES

1. D. A. Benaron, S. R. Hintz, A. Villringer, D. Boas, A. Kleinschmidt, J. Frahm, C. Hirth, H. Obrig, J. C. Van Houten, E. L. Kermit, W. Cheong, D. K. Stevenson, Noninvasive functional imaging of human brain using light, *J. Cerebral Blood Flow and Metabolism* **20**, 469-477 (2000).
2. Y. Hoshi, I. Oda, Y. Wada, Y. Ito, Y. Yamashita, M. Oda, K. Ohta, Y. Yamada, M. Tamura, Visuospatial imagery is a fruitful strategy for the digit span backward task: a study with near-infrared optical tomography, *Cognitive Brain Research* **9**, 339-342 (2000).
3. E. Watanabe, A. Maki, F. Kawaguchi, Y. Yamashita, H. Koizumi, Y. Mayanagi, Noninvasive cerebral blood volume measurement during seizures using multichannel near infrared spectroscopic topography, *J. Biomed. Opt.* **5**, 287-290 (2000).
4. M. Franceschini, V. Toronov, M. E. Filiaci, E. Gratton, S. Fantini, On-line optical imaging of the human brain with 160-ms temporal resolution, *Optics Express* **6**, 49-57 (2000).

5. S. Fantini, D. Huebert, M. A. Franceschini, E. Gratton, W. Rosenfeld, P. G. Stubblefield, D. Maulik, and M. Stankovic, Non-invasive optical monitoring of the newborn piglet brain using continuous-wave and frequency-domain spectroscopy, *Phys. Med. Biol.* **44**, 1543-1563 (1999).
6. M. R. Stankovic, D. Maulik, W. Rosenfeld, P. G. Stubblefield, A. D. Kofinas, S. Drexler, R. Nair, M. A. Franceschini, D. Hueber, E. Gratton, and S. Fantini, Real-time optical imaging of experimental brain ischemia and hemorrhage in neonatal piglets, *J. Perinat. Med.* **27**, 279-286, 1999.
7. H. Koizumi, Y. Yamashita, A. Maki, T. Yamamoto, Y. Ito, H. Itagaki, and R. Kennan, Higher-Order Brain Function Analysis by trans-cranial dynamic near-infrared spectroscopy imaging, *J. Biomed. Opt.* **4**, 403-413 (1999).
8. A. Villringer and B. Chance, Non-invasive optical spectroscopy and imaging of human brain function, *Trends Neuroscience* **20**, 435-442 (1997).
9. M. Tamura, Y. Hoshi, and F. Okada, "Localized near-infrared spectroscopy and functional optical imaging of brain activity," *Philosophical Transactions of the Royal Society of London - Series B: Biological Sciences* **352**(1354), 737-42, (1997).
10. A. Kleinschmidt, Hellmuth Obrig, M. Requardt, K. Merboldt, U. Dirnagl, A. Villringer, and J. Frahm, Simultaneous recording of cerebral blood oxygenation changes during human brain activation by magnetic resonance imaging and near infrared spectroscopy, *J. Cerebral Blood Flow and Metabolism* **16**, 817-826 (1996).
11. H. Liu, B. Chance, A. H. Hielscher, S. L. Jacques, F. K. Tittel, Influence of blood vessels on the measurement of hemoglobin oxygenation as determined by time-resolved reflectance spectroscopy, *Med. Phys.* **22**, 1209-1217 (1995).
12. G. Gratton and M. Fabiani, Dynamic brain imaging: Event-related optical signal (EROS) measures of the time course and localization of cognitive-related activity, *Psychonomic Bulletin and Review* **5**, 535-563, (1995).
13. A. Maki, Y. Yamashita, Y. Ito, E. Watanabe, Y. Mayanagi, H. Koizumi, Spatial and temporal analysis of human motor activity using non-invasive NIR topography, *J. Med. Phys.* **22**, 1997-2005 (1995).
14. Y. Hoshi and M. Tamura, Detection of dynamic changes in cerebral oxygenation coupled to neuronal function during mental work in man, *Neuroscience Letters* **150**, 5-8 (1993).
15. Hintz S.R., W.F. Cheong, J.P. van Houten, D.K. Stevenson, D.A. Benaron, Bedside imaging of intracranial hemorrhage in the neonate using light: comparison with ultrasound, computed tomography, and magnetic resonance imaging, *Pediatr. Res.* **45**, 54-59 (1999).
16. A.H. Hielscher, A. D. Klose, K. M. Hanson, Gradient-based iterative image reconstruction scheme for time-resolved optical tomography, *IEEE Trans Med Imag.* **18**, 262-271 (1999).
17. A.D. Klose, and A.H. Hielscher, Iterative reconstruction scheme for optical tomography based on the equation of radiative transfer, *Med. Phys.* **26**, 1698-1707 (1999).
18. R. Roy and E. M. Sevick-Muraca, Truncated Newton's optimization scheme for absorption and fluorescence optical tomography: Part I Theory and formulation, *Optics Express* **4**, 353-371 (1999).
19. S.R. Arridge, M. Schweiger, A gradient-based optimization scheme for optical tomography, *Optics Express* **2**, 213-226 (1998).
20. M. Schweiger, S.R. Arridge, M. Hiraoka, D.T. Delpy, The finite element model for the propagation of light in scattering media: Boundary and source conditions, *Med. Phys.* **22**, 1779-92 (1995).
21. S.R. Arridge, M. Schweiger, M. Hiraoka, D.T. Delpy, A finite element approach for modeling photon transport in tissue, *Med. Phys.* **20**, 299-309 (1993).
22. G. Abdoulaev, A. Varone and G. Zanetti, An object oriented flow solver for the CRS4 virtual vascular project, in Proc. Of the 3rd European Conf. on Numerical Mathematics and Advanced Applications, P. Neittaanmaki, T. Tiihonen and P. Tarvainen (eds.) (World Scientific, Singapore), 407-415 (2000).
23. J. H. Bramble, J. E. Pasciak, and J. Xu, Parallel multilevel preconditioners, *Math. Comp.* **55**, 1-22 (1990).
24. Y. Pei, H.L. Graber, R.L. Barbour, Influence of systematic errors in reference states on image quality and on stability of derived information for DC optical imaging, *Applied Optics* (2001) in press.
25. D.A. Boas, T. Gaudette, G. Strangman, X. Cheng, J.J. Marota, J.B. Mandeville, The accuracy of near infrared spectroscopy and imaging during focal changes in cerebral hemodynamics, *Neuroimage* **13**, 76-90 (2001).
26. A. J. Davies, D. B. Christianson, L. C. W. Dixon, R. Roy, and P. van der Zee, Reverse differentiation and the inverse diffusion problem, *Advances in Engineering Software* **28**, 217-221 (1997).
27. D.B. Christianson, A. J. Davies, L. C. W. Dixon, R. Roy, P. Van der zee, Giving Reverse Differentiation a Helping Hand, *Optimization Methods and Software* **8**, 53-67 (1997).

28. H. M. Karara, *Handbook of Non-topographic Photogrammetry* (American Society of Photogrammetry, Falls Church, VA, 1989).
29. E. F. Church, *Elements of Photogrammetry* (Syracuse University Press, New York, 1948).
30. G. Deng, W. Falg, An evaluation of an off-the-shelf digital close-range photogrammetric software package, *Photogrammetric Engineering and Remote Sensing* **67**, 227-233 (2001).
31. R.H. Bartels, J.C. Beatty, and B.A. Barsky, *An Introduction to Splines for Use in Computer Graphics and Geometric Modeling* (Morgan Kaufman Publishers, 1987).
32. A. Bluestone, G. Abdoulaev, R.L. Barbour, C.H. Schmitz, A.H. Hielscher, "Three-dimensional optical-tomographic localization of changes in absorption coefficients in the human brain," in *Optical Tomography and Spectroscopy of Tissue IV*, SPIE-Proceedings 4250, Bellingham, WA, 258-268 (2001).
33. C.H. Schmitz, H.L. Graber, H. Luo, I. Arif, J. Ira, Y. Pei, A. Bluestone, S. Zhong, R. Andronica, I. Soller, N. Ramirez, S.L.S. Barbour, and R.L. Barbour, Instrumentation and calibration protocol for imaging dynamic features in dense scattering media by optical tomography, *Appl. Opt.* **39**, 6466-6485 (2000).
34. C.H. Schmitz, M. Lcker, J. Lasker, A.H. Hielscher, R.L. Barbour, "Performance characteristics of a silicon-photodiode-based instrument for fast functional optical tomography," in *Optical Tomography and Spectroscopy of Tissue IV*, SPIE-Proceedings 4250, Bellingham, WA, 171-179 (2001).
35. F. P. Tiecks, C. Douville, S. Byrd, A. M. Lam, D. W. Newell, Evaluation of impaired cerebral autoregulation by the Valsalva Maneuver, *Stroke* **27**, 1177-1182 (1996).
36. X. Cheng, D.A. Boas, Systematic diffuse optical image errors resulting from uncertainty in the background optical properties, *Optics Express* **4**, 299-307 (1999).
37. S. Wray, M. Cope, D.T. Delpy, Characteristics of the near infrared absorption spectra of cytochrome aa₃ and hemoglobin for the noninvasive monitoring of cerebral oxygenation, *Biochim Biophys Acta* **933**, 184-192 (1988).
38. J.E. Raising, G.W. Kindt, J.E. McGillicuddy, S.L. Giannotta, The effects of primary elevation of cerebral venous pressure on cerebral hemodynamics and intracranial pressure, *J. Surg. Res.* **26**, 101-107 (1979).